

SYSTEM DESCRIPTION AND INITIAL PERFORMANCE RESULTS FOR BEAMLET

B. M. Van Wonterghem

C. E. Barker

J. R. Murray

I. C. Smith

J. H. Campbell

D. F. Browning

D. R. Speck

W. C. Behrendt

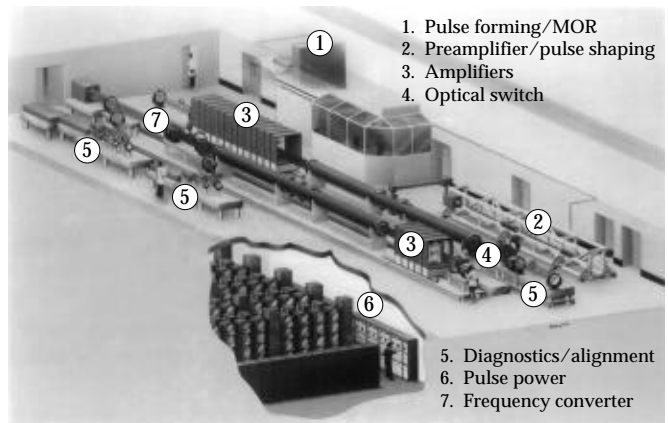
Introduction

The Department of Energy has proposed to design and construct a National Ignition Facility (NIF) for Inertial Confinement Fusion (ICF) research. This facility will contain a frequency-tripled, Nd:Glass laser system capable of irradiating fusion targets at an energy and power of 1.8 MJ and 500 TW. The laser output pulse contains most of the energy, where the low-intensity leading foot is 15–20 ns long and the final high-intensity pulse is 3–4 ns long. The laser will have 192 independent “beamlets,” each having a final square clear aperture of $40 \times 40 \text{ cm}^2$ and an output beam area slightly smaller than the clear aperture. A Conceptual Design Report (CDR),¹ prepared in May 1994, discusses the laser and facility design in detail.

We have constructed and are now testing a scientific prototype of a single beamlet of the proposed NIF laser (Fig. 1). The purpose of these tests is to show that the novel features proposed for the NIF laser design will perform as projected and that the laser is ready for final engineering design. The final dimensions and component arrangements for NIF will differ somewhat from our scientific prototype, but the differences are sufficiently small that tests on the prototype can be used to demonstrate performance essentially equivalent to a NIF beamlet.

The project to build a scientific prototype beamlet (hereafter referred to as “Beamlet”) was begun in 1991 and consisted of three main efforts: (1) development of laser components, (2) design and construction of the main laser system, and (3) activation. Previous *Quarterlies* present the results of the component development activities^{2–5} and the laser design.⁶ This article presents an overview of the constructed Beamlet laser system, and the results from the first integrated tests performed near the end of laser activation. These integrated tests culminated in a third-harmonic milestone shot on

(a) Beamlet laser



(b) Fully assembled system



FIGURE 1. (a) Artist's rendering of the Beamlet laser showing the main subsystems. (b) A photograph of the fully assembled system. (70-50-0195-0181pb01)

September 8, 1994 that produced an average output 3 ω fluence of 8.7 J/cm² in a 29.6 \times 29.6 cm² beam and a 3-ns square pulse. Table 1 summarizes the key energy and fluence performance results recently achieved on Beamlet at 1 ω and 3 ω . The fluence levels listed in Table 1 (and discussed later in this article) are higher than the fluences projected for the NIF design.¹

Subsequent articles in this *Quarterly* present detailed design and test results for many of the major components on Beamlet. The final article compares the results of the performance of Beamlet with recent model calculations.

The NIF Laser Design Compared with Current ICF Lasers

Figure 2 shows the singlepass master oscillator/power amplifier (MOPA) architecture; Fig. 3 shows the multipass architecture proposed for the NIF laser and contrasts that with the prototype Beamlet design.¹

Current ICF Laser Design—A Singlepass Architecture

Most large glass lasers designed for inertial fusion experiments have the singlepass MOPA architecture: the Nova laser⁷ at Lawrence Livermore National Laboratory (LLNL), USA; the Omega laser⁸ at the

Laboratory for Laser Energetics, University of Rochester, USA; the Gekko XII laser⁹ at the Institute of Laser Engineering, University of Osaka, Japan; the Phébus laser¹⁰ at the Commissariat à l'Énergie Atomique, Centre d'Études de Limeil-Valenton, France; and the Helen laser at the Atomic Weapons Research Establishment, England.

A master oscillator generates a few-nanosecond pulse of several millijoules that is then spatially and temporally shaped at about a 1-cm aperture and split into parallel chains of singlepass rod and Brewster's-angle slab amplifiers of increasing size. Gain isolation is provided at small aperture (<~10 cm) by ring-electrode Pockels cells and thin-film polarizers. Faraday rotators, driven by pulsed electromagnets, are used at large apertures to isolate pulses from propagating backward down the laser chain. Single-beam amplifiers with round apertures up to about 32 cm are used in all of these facilities. In addition, Nova and Phébus lasers have amplifiers with apertures of 46 cm using glass slabs that are split into two independent pieces.

The singlepass MOPA is a familiar and well-proven design that can be assembled and tested in stages, so performance risk is low. Cost and complexity are high, however, because of the very large number and variety of components required for a MOPA design. The Nova laser, for example, contains one rod amplifier

FIGURE 2. Singlepass master-oscillator, power-amplifier (MOPA) laser architecture commonly used by existing ICF lasers. (40-00-0294-0375pb01)

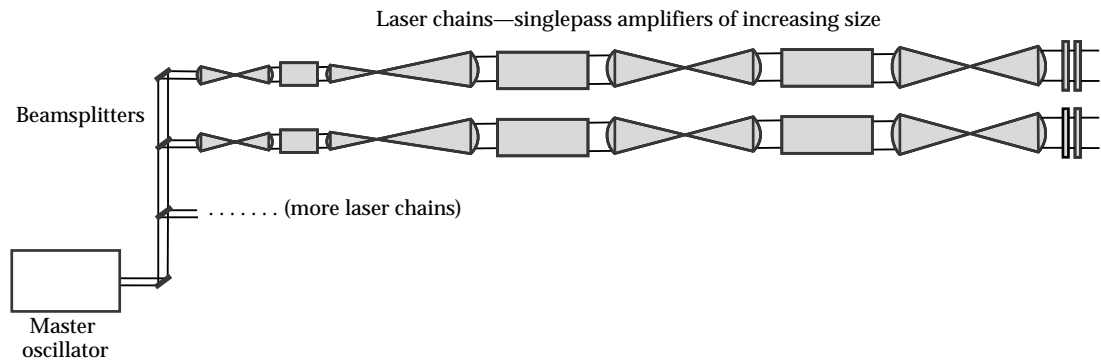


TABLE 1. Initial performance results for the NIF prototype beamlet at 1054 and 351 nm.

Wavelength (nm)	Zero-intensity beam dimensions (cm ²)	Output ^a pulse length (ns)	Fluence (J/cm ²)	Total energy (kJ)	Spatial intensity modulation (pk-avg) ^b
1054	34 \times 34	3	12.5	12.1	1.45:1
		5	14.3	13.9	1.25:1
		8	16	15.5	1.25:1
351	29.6 \times 29.6	3	8.7	6.4	1.35:1

^aTemporally square output pulse.

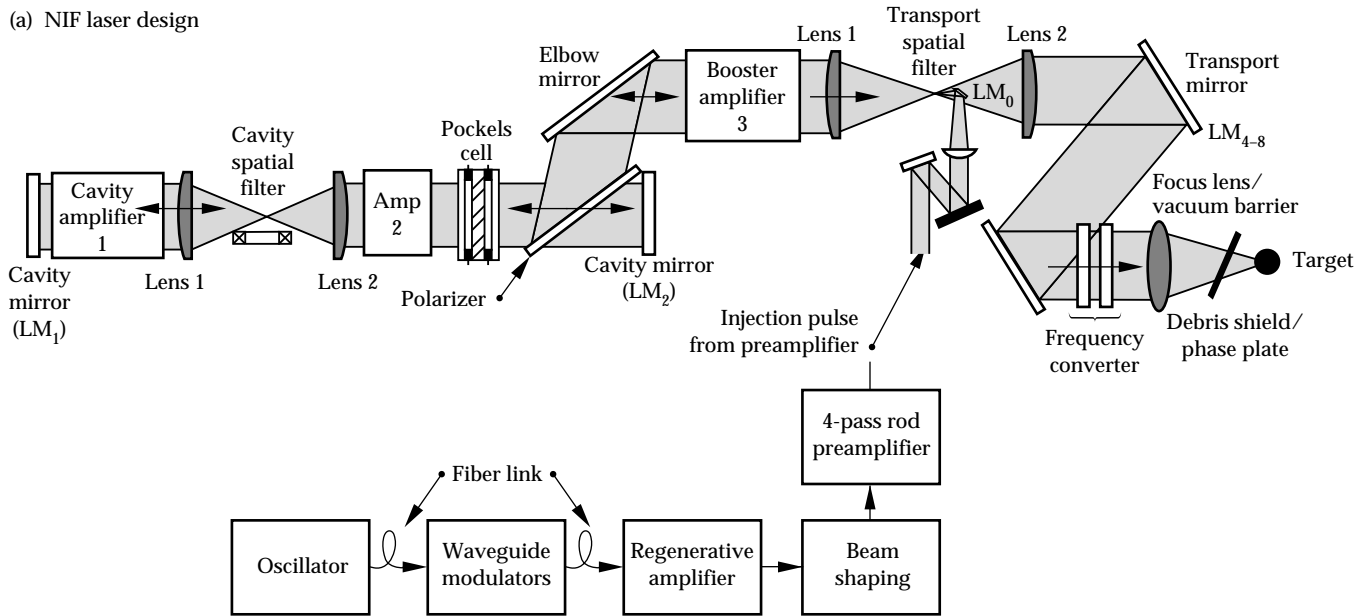
^bPeak-to-average ratio.

and five sizes of elliptically shaped slab amplifiers (a total of 41 slabs) in each of ten laser chains. There are also eight additional rod amplifiers of several sizes between the oscillator and the chains. In addition, there are relay telescopes and isolators between all of these amplifier stages.

The existing ICF MOPA lasers were all designed for maximum effective operation at pulse lengths near 1 ns. Fusion targets for the NIF, however, require effective pulse lengths typically in the range of 3–5 ns. If the

laser design pulse length increases above 1 ns then the corresponding increase in component damage thresholds allows the laser to operate at higher fluences. This significantly increases the efficiency of energy extraction from the laser glass. In the case of the MOPA design, however, these high extraction fluences produce significant gain saturation in the large amplifiers. This, in turn, requires that the successive MOPA amplifiers have increasingly larger apertures so they do not gain-saturate, since gain-saturation effects produce

(a) NIF laser design



(b) Prototype Beamlet

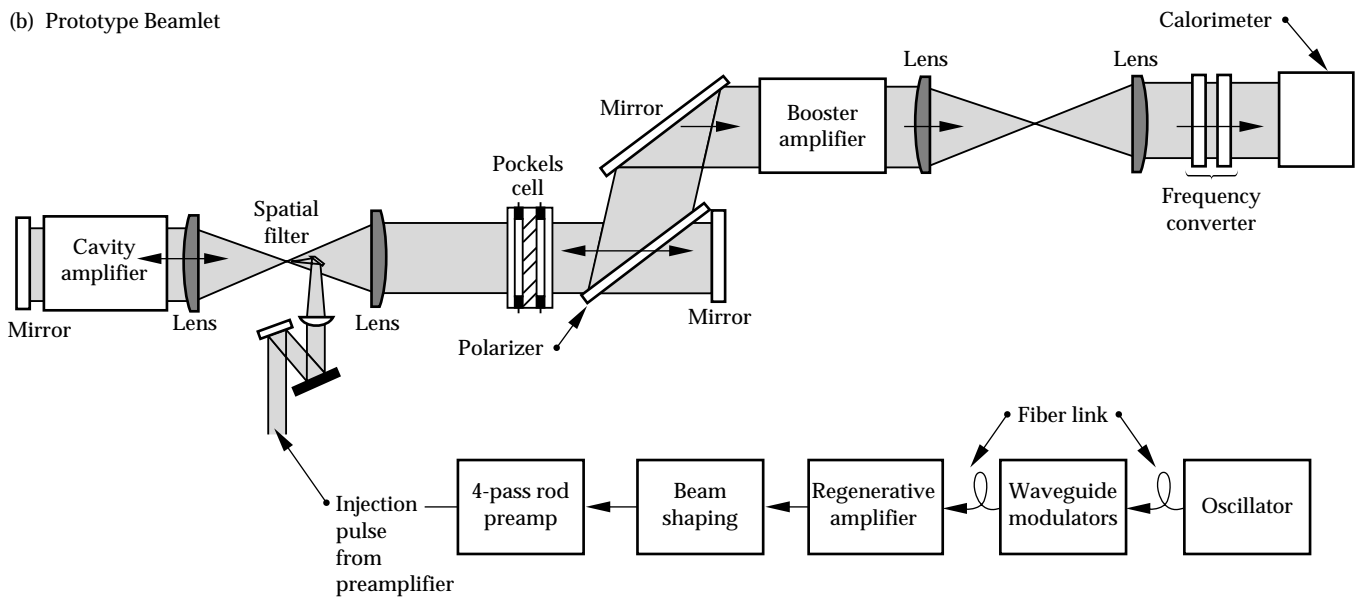


FIGURE 3. (a) Schematic drawing of the multipass NIF laser design. (b) Prototype Beamlet design. (40-00-0394-0789pb02)

severe temporal pulse distortion. (See “Beamlet Pulsed-Power System,” p. 62). In contrast, a multipass amplifier uses the full aperture of the main amplifier as a preamplifier on early passes, such that the fluence increases monotonically during propagation, reaching a maximum of several times the saturation fluence in the last slab of the booster amplifier. Temporal pulse distortion is minimized in this configuration.

NIF/Beamlet—A Large-Aperture, Multipass Laser Design

In the NIF design [Fig. 3(a)], the pulse-forming system uses a low-power oscillator to drive an array of single-mode optical fibers, one for each beamlet of the system (the prototype Beamlet oscillator drives only a single fiber). The output from each fiber is input to waveguide-amplitude modulators to temporally shape the pulse and then fed to phase modulators to add the required bandwidth (bandwidth is required to suppress stimulated Brillouin scattering, or SBS, in the output optics when driven at high intensities). These integrated optical modulators are derived from the low-voltage designs used in high-speed fiber communications networks, and ultimately could be operated under direct computer

control, although Beamlet has not yet implemented this option. The pulse output from the modulator is then fed to a single-mode, regenerative amplifier that amplifies the pulse to ~ 10 mJ.³ A beam-shaping section forms the appropriate spatial intensity profile that is injected into the preamplifier section of the laser amplifier chain. A four-pass, single-rod preamplifier amplifies the pulse to about 1 J and injects it into the main four-pass slab amplifier, where it reaches approximately 10 kJ. The four-pass configuration permits us to make the preamplifier section small enough that the cost savings from any further reduction would be negligible. The prototype Beamlet uses 16 rectangular slabs in the final amplifier stage that have a pumped aperture of 39 cm. The pulse that exits the laser amplifier section proceeds to a frequency converter and, in the case of the NIF, to the target chamber.

A multipass amplifier requires a method for separating input and output beams in the amplifier, which is not necessary in a singlepass system. There are three generic techniques for accomplishing this: (1) a polarization rotator can be used to separate beams at a polarizer [Fig. 4(a)]; (2) the beams can be separated in angle in the near field [Fig. 4(b)]; or (3) they can be separated in angle in the far field near a focal plane [Fig. 4(c)]. Near-field angle separation has been used with large laser systems.¹¹ It requires either a very long propagation distance, leading to difficulties with diffraction, or a beam size much smaller than the amplifier aperture to accommodate the beam motion, leading to poor utilization of the amplifier volume. Therefore, near-field separation has not been considered for the NIF design.

Far-field angle separation has several desirable features for this application. There is no closed path in the laser cavity, so parasitic oscillations are less of an issue than for a configuration in which there are closed resonant feedback paths. Each pass through the focal plane goes through a separate aperture in that plane, so the propagation of later passes is not affected by plasma generated in the aperture by earlier passes. Any leakage out of the cavity on early passes is at an angle to the final output beam, so it is easily occluded in a transport spatial filter and cannot disturb the laser target. Finally, far-field angular separation gives a convenient location for injecting a low-energy input pulse near the focal plane without requiring additional full-aperture optical components.

The Beamlet test series presented here uses a combination of far-field angle plus polarization separation. Polarization separation is achieved using a full-aperture Pockels cell plus a polarizer in the large final amplifier stage. The far-field angle separation gives the advantages

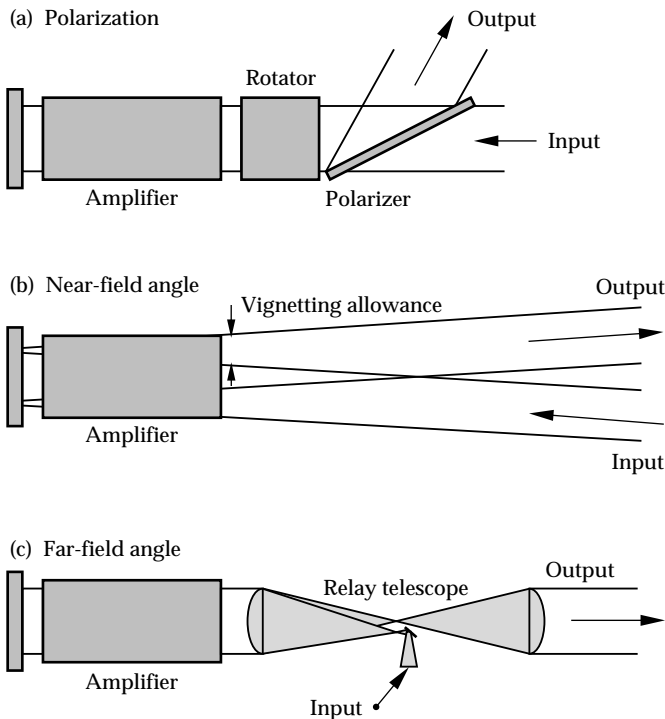


FIGURE 4. Three generic schemes for separating the input and output beams for a multipass laser architecture: (a) polarization rotator and polarizer, (b) near-field angle separation, and (c) far-field angle separation. NIF and the prototype Beamlet use a combination of far-field angle separation and polarization rotator. (70-50-0195-0020pb01)

just mentioned, while the Pockels cell gives gain isolation and isolation from back reflections. The full-aperture Pockels cell also allows the off-axis angle in the far-field to be very small since, at that point, the energy handled on the injection optics is only about 1 J. The small angle allows efficient use of the amplifier aperture with a relatively short laser cavity. It is possible to configure the system to do separation using a far-field angle only, using a smaller Pockels cell for isolation purposes only. This alternate configuration requires handling the beam near the far field and at energies up to 100 J, but avoids the cost of the full-aperture Pockels cell and polarizer. Both configurations will be tested on Beamlet.

The NIF laser design groups beamlet amplifiers into large arrays stacked four high and twelve wide to minimize the number of components and flash lamps (see Fig. 1 in “Design and Performance of the Beamlet Amplifiers,” p. 18). The individual beamlets are optically independent, though supported by common mechanical hardware and pumped by common flash lamps. This full array of 48 apertures is too large and expensive to test in a small scientific prototyping effort. Therefore, on Beamlet we constructed the amplifier as an array of four apertures stacked two high and two wide to study many of the major issues of this type of amplifier assembly. (See “Design and Performance of the Beamlet Amplifiers,” p. 18.) Only one of the four beamlet apertures contains high-quality laser glass and is used for the tests discussed here. The amplifiers are constrained to have an odd number of slabs, since this cancels asymmetric gain gradients in the two end slabs.

A state-of-the-art adaptive wavefront control system is used on Beamlet to correct for static and dynamic optical aberrations. The Beamlet adaptive optic system

consists of a deformable mirror (DFM), two Hartmann wavefront sensors, and a closed-loop controller. This adaptive optic technology was developed and demonstrated on the large dye laser systems that are part of the LLNL Uranium-Isotope Separation project.¹² The Beamlet adaptive optics system is discussed further in “Beamlet Pulse-Generation and Wavefront-Control System,” p. 42.

The amplifier stages are separated by relay telescopes or spatial filters that reimage a beam-forming aperture at several places through the amplifier chain. This reimaging reduces the diffractive growth of spatial intensity noise and provides Fourier transform planes at the focal planes in the telescopes where high-spatial-frequency intensity noise can be reset to zero. The noise level needs to be kept low because nonlinear propagation effects cause it to grow exponentially at high intensity.¹

Beamlet Test Configuration

Figure 5 is a plan view of Beamlet as configured for the test series presented here. We use a prototype³ of the pulse generation and preamplifier system proposed for NIF to produce an approximately 1-J pulse that is injected into the main four-pass laser cavity. The injected pulse is temporally shaped to compensate for gain saturation effects and is designed to produce a 3-ns square pulse output. To compensate for gain roll-off near the edges of the amplifier slabs, the intensity profile is shaped using a transmission filter with a parabolic transmission profile (see “Beamlet Pulse-Generation and Wavefront-Control System,” p. 42). Also, all laser experiments reported here use input pulses that are phase-modulated

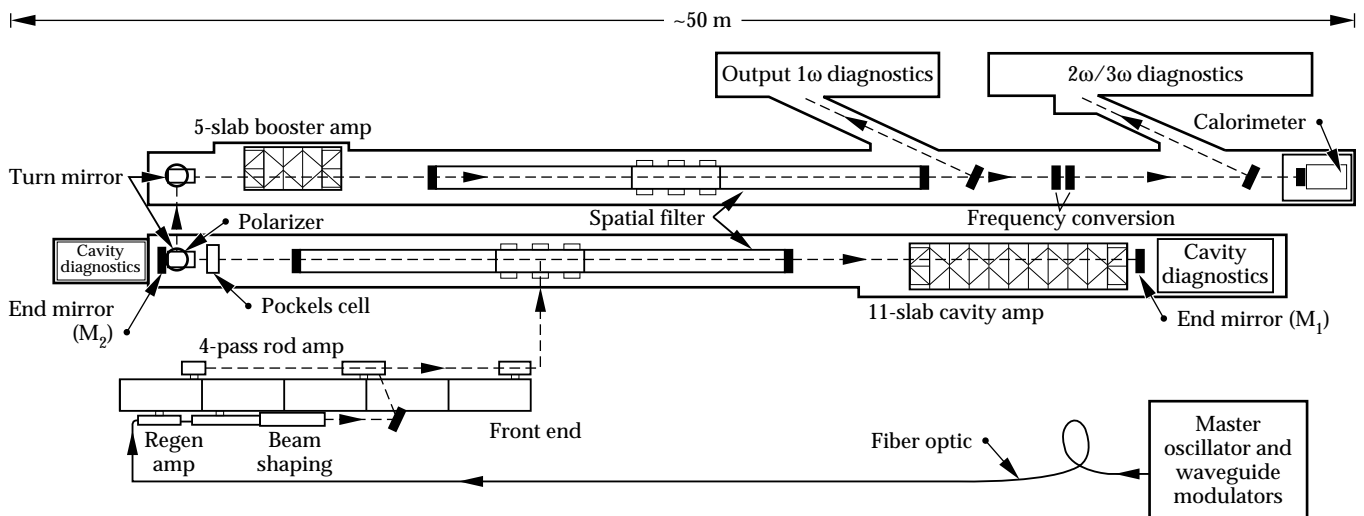


FIGURE 5. Plan view of Beamlet as configured for the tests described in this article. (02-30-1091-3760Epb01)

by the front end at a single modulation frequency of 5 GHz to provide a total bandwidth of about 30 GHz. This additional bandwidth reduces the net SBS gain, thus eliminating the damage threat posed by transverse SBS. The output pulse from the front end is injected using a small $2 \times 2 \text{ cm}^2$ 45° mirror, and the pulse comes to a focus at an aperture in the focal plane of a vacuum spatial filter. The pulse expands past focus to fill a recollimating lens and a multisegment amplifier² containing eleven Brewster's-angle slabs. (See the article "Design and Performance of Beamlet Amplifiers," p. 18.) It then reflects from a cavity end mirror M_1 , and makes a second pass through the multipass amplifier, emerging with an energy of about 100 J.

At the other end of the laser cavity is an optical switch, consisting of a plasma-electrode Pockels cell (PEPC) and a polarizer. (See Ref. 4 and "Design and Performance of the Beamlet Optical Switch," p. 29 for a discussion of optical switches; see "Large-Aperture, High-Damage Threshold Optics for Beamlet," p. 52 for a discussion of polarizers.) As the pulse is injected for its first two passes through the multipass amplifier, the Pockels cell is switched on to rotate the polarization so that the pulse passes through the polarizer and strikes a second mirror, M_2 . It then returns to the multipass amplifier for a third and fourth pass, emerging with an energy near 6 kJ. By the time it returns to the Pockels cell, the cell has switched off, so the pulse then reflects from the polarizer and makes a single pass through a second so-called "booster" amplifier containing five Brewster's-angle slabs. A transport spatial filter relays the pulse to the frequency converter. At this point, the 1ω energy is 12–15 kJ, as shown in Table 1.

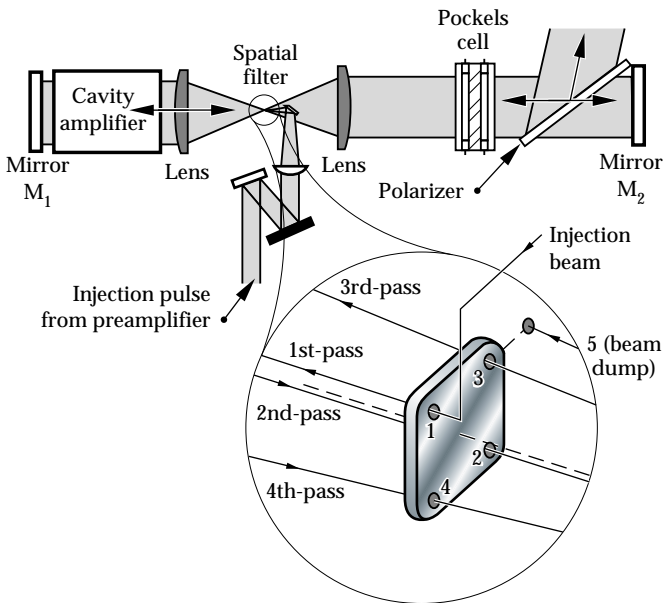


FIGURE 6. Pinhole array layout at the focal plane of the Beamlet multipass cavity. (70-50-0393-0724Bpb01)

Figure 6 is a schematic of the array of pinhole apertures at the focal plane of the cavity spatial filter. Mirror M_1 is positioned such that the pulse injected at pinhole 1 returns to a position at pinhole 2. Similarly, mirror M_2 is aligned so that the return pulse from M_2 is at pinhole position 3. The return from the second pass then automatically lies at pinhole 4. Any energy not switched out of the cavity strikes mirror M_2 and returns to the focal plane at position 5 where it is intercepted by an absorbing glass beam dump. For this series of experiments, we used 3.6-mm-diam pinhole apertures, giving a spatial frequency cutoff wavelength of 7.2 mm in the near field, or an angular acceptance of $\pm 200 \mu\text{rad}$ in the far field. The separation between pinhole apertures is 3 cm.

The clear aperture of the potassium dihydrogen phosphate (KDP) crystal installed in the Pockels cell for the 1ω tests is 37 cm, which sets a beam hard aperture of about 35 cm. The beam must be smaller than the smallest clear aperture because of the vignetting allowance for beam motion due to off-axis propagation plus an allowance for full-beam alignment. The edge of the beam is apodized to suppress edge diffraction, as discussed later. The 39-cm amplifier aperture is not completely filled under these conditions, and could support slightly larger beam dimensions.

The cavity spatial filter lenses have a focal length of 9 m. The separation between M_1 and M_2 is 36 m and these mirrors lie at relay image planes of the system.

The beam is reflected out of the multipass cavity by the switch polarizer and then routed to the booster amplifier using three turning mirrors. After passing through a second spatial filter identical to the one in the multipass cavity, the beam then passes through an uncoated fused silica beamsplitter. The beamsplitter reflects a small portion of the $1\text{-}\mu\text{m}$ output beam to a diagnostics package. This package captures near- and far-field images on charge-coupled device (CCD) cameras, determines the energy using a calorimeter, and measures the temporal pulse shape using a vacuum photodiode with a transient digitizer or a streak camera. It also includes a 77-element CCD-based Hartmann sensor to measure wavefront distortion and to control the figure of the 39-actuator DFM.

The 1ω output beam enters a dual crystal frequency converter. The frequency converter uses a Type I/II third-harmonic generation scheme (Fig. 7), consisting of a 1.05-cm-thick KDP doubler crystal and a 0.95-cm-thick KD*P tripler crystal. In the experiments described here, $32 \times 32 \text{ cm}^2$ crystals were used and the KD*P was 80% deuterated. The $32 \times 32 \text{ cm}^2$ crystals will support about a 30-cm beam size. Crystals $37 \times 37 \text{ cm}^2$ are currently being manufactured and will be used in future experiments. (Due to the long time required to grow the $37 \times 37 \text{ cm}^2$ crystal boules, these larger crystals

were not available during our initial frequency conversion tests.) Finally, the output beam is absorbed by a $74 \times 74 \text{ cm}^2$ calorimeter/beam dump after first passing through a biconcave expansion lens to reduce the fluence onto the calorimeter below the damage threshold of the absorbing glass in the calorimeter.

Measurement of Laser Performance at $1.05 \mu\text{m}$

Optical Transmission with Unpumped Amplifiers

Optical losses reduce the laser output, particularly with long pulses where the laser amplifier gain is highly saturated. It is important to quantify these losses to match the measured laser output to theoretical models. We measured transmission through the system with unpumped amplifiers from pinhole to pinhole of the spatial filters, and also measured individual components to determine what these optical losses are for the Beamlet.

The transmission for a double pass through the eleven-slab-long cavity amplifier section is 84%, which consists of 22 laser slabs having an average transmission of 99.3%, one mirror with 99.6% reflection, and two lens transmissions at 99% each. The 0.5% loss per lens surface is typical of sol-gel antireflection coatings applied to fused silica, although coatings as good as 99.8% transmission have been prepared. The loss in laser slab transmission is dominated by absorption from the Boltzman population in the lower Nd:Glass

laser level, and illustrates that bulk and surface losses due to contamination or defects in the laser glass are extremely small.

The double-pass transmission through the Pockels cell (in its “on” position) plus the polarizer is 71%. The crystal in the Pockels cell is 1-cm-thick undeuterated KDP (KH_2PO_4), so it has an absorption of 6%/cm at $1.053 \mu\text{m}$, giving a double-pass transmission of 88%. The polarizer singlepass transmission for *p*-polarized light is 97.3%. This includes 1.1% loss due to the 9-cm-thick BK-7 substrate and 1.5% loss in the coating. If we assume 1% loss per surface for 16 antireflection coated surfaces (a lens, two windows, and a KDP crystal) and a mirror reflection of 0.995, the net transmission would be 71%, which is consistent with the measured value. (See “Design and Performance of the Beamlet Optical Switch,” p. 29 for a more detailed discussion of the optical performance of the Pockels cell.)

The transmission of amplifier slabs in the booster and lenses in the output spatial filter are consistent with the measurements for the cavity amplifier and spatial filter discussed earlier. The polarizer reflects 99.6% of the *s*-polarized light that strikes it when the Pockels cell is switched to its “off” configuration. At an output energy of $\sim 12 \text{ kJ}$ after the booster amplifier, the polarizer reflects 6 kJ out of the multipass cavity and the energy transmitted through the polarizer is less than 30 J (polarizer *s*-polarized leakage plus any light rotated to *p*-polarization by birefringence in the system).

Gain Compensation

Figure 8 shows the singlepass, small-signal gain profile of a five-slab-long Beamlet amplifier pumped to

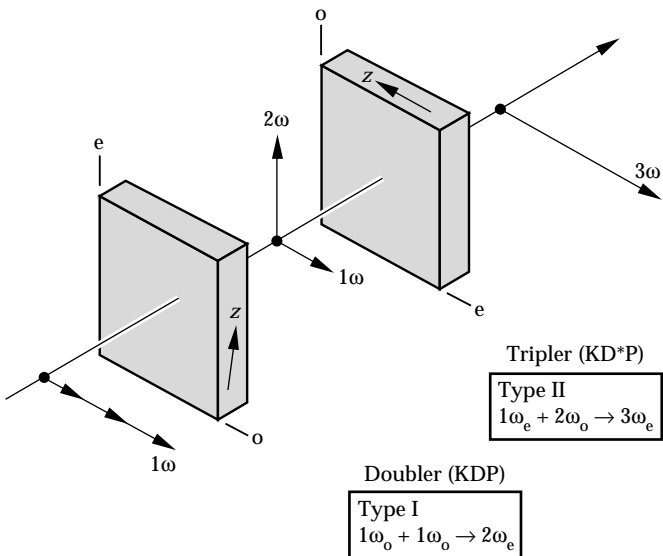


FIGURE 7. Type I/II frequency conversion scheme used on Beamlet. (70-10-0494-1827pb01)

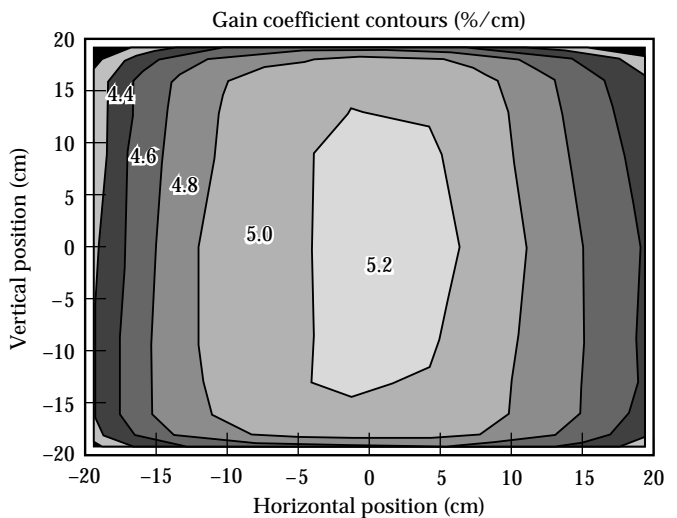


FIGURE 8. Gain profile for a five-slab-long amplifier. Amplified spontaneous emission causes the gain to roll off near the edges in the horizontal direction of the slabs. (02-30-1093-3495pb01)

its nominal operating point, 20% of the flash-lamp explosion energy. The gain peaks in the center of the aperture and is about 15% lower in the extreme corners of the aperture. Most of the gain roll-off is in the horizontal direction, which is the long dimension of the Brewster's-angle slab. Amplified spontaneous emission trapped by total internal reflection within the slab depletes the stored energy in the glass and causes this gain roll-off. (See "Design and Performance of the Beamlet Amplifiers," p. 18.)

To produce a flat intensity profile at the output of the laser requires that the input intensity profile to the multipass amplifier stage be shaped to compensate for the nonuniform gain profile in the horizontal direction (the effect of the vertical gain profile is insignificant). The input intensity profile used for the results presented here is parabolic in the horizontal direction with the edges of the aperture twice as intense as the center. Figure 9 shows the output intensity profile in the horizontal direction from the multipass stage only (without the booster amplifier) showing the effect of the gain compensation on the horizontal intensity profile. Note that without compensation for the gain distribution, the intensity near the edges of the beam rolls off

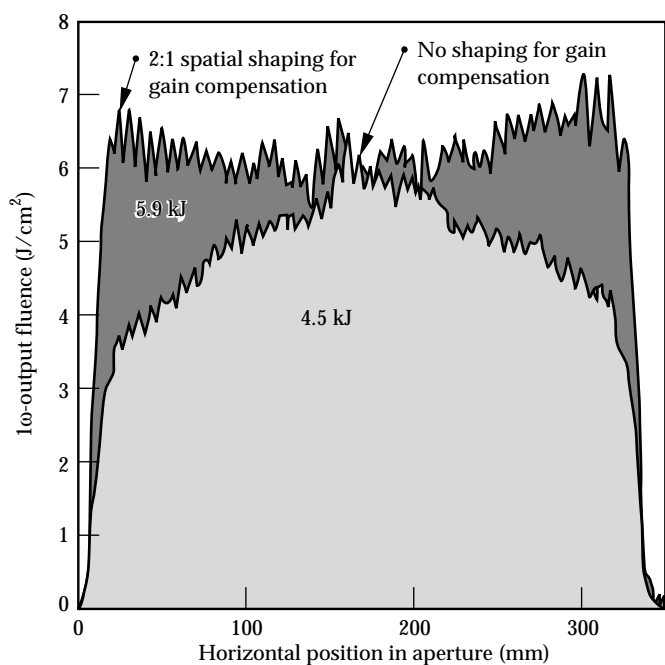


FIGURE 9. Effect of gain compensation on the horizontal intensity profile after four passes through the main multipass cavity. By compensating for the horizontal gain roll-off in the amplifier, the extracted energy increases 30%, and the output has the desired flat-top shape. (70-50-0494-2115pb02)

dramatically. However, with gain compensation, a nearly flat, top-hat-shaped intensity profile is obtained. This is very important because the performance is limited by the peak laser fluence on the optical components. Therefore a flat beam profile allows a higher output energy at equal peak fluence: the gain-compensated profile has nearly 30% greater energy extraction for the same peak fluence.

Edge Apodization and Fill Factor

It is important to fill the beam aperture as fully as possible to maximize the flat-top portion of the beam area and hence the laser output energy. A 1-cm margin around the edge of a nominal $34 \times 34 \text{ cm}^2$ beam contains 11% of the beam area, so changes of only a few millimeters in beam dimensions can have a noticeable impact on the output energy of the system. Edge diffraction from sharp beam edges causes intensity peaks on the beam, however, so the beam intensity at the edge must be apodized. (That is, the intensity must decrease smoothly to zero over a region occupying at least a few Fresnel zones over the propagation distances for which these intensity peaks are not acceptable.)

The edge apodization used in the 1ω tests is an inverted Gaussian profile with the 10^{-2} intensity point at a square aperture of $34 \times 34 \text{ cm}^2$.¹³ (For the 3ω tests, we used a smaller square beam size of $29.6 \times 29.6 \text{ cm}^2$.) The 10^{-2} intensity point is considered the "zero intensity" level and is the maximum intensity allowed to strike the edges of the clear aperture of optical components. The corners of the beam are rounded with a radius of 5 cm to suppress diffraction from these regions; this subtracts 20 cm^2 from the beam area.

The 1ω output beam with a zero intensity width of 34 cm has a half-power width of 31.5 cm when the laser is operated under heavily saturated conditions. The flat-top, high-intensity region in the center is 30.6 cm wide. The experimental data show no growth of diffractive intensity peaks around the edge of the beam, though simulations suggest that there is some growth under high-fluence and high-B conditions near the end of the pulse. We project, from simulations, that it should be possible to steepen the edge profile and reduce the edge apodization region by approximately half a centimeter with acceptable diffractive intensity growth. (This will be tested during future experiments on Beamlet.) The effective beam area at half power is 971 cm^2 after allowing for the 20 cm^2 loss in the corners, and we use that value to calculate fluence and intensity in the flat-top portion of the beam. The "fill factor" is 84% (defined as the ratio of the beam energy to the energy if the entire $34 \times 34 \text{ cm}^2$ hard aperture were filled at the fluence of the flat central area of the beam).

Energy Performance

Figure 10 shows the Beamlet 1ω output energy that goes to the frequency converter as a function of energy injected into the main four-pass amplifier cavity. The solid line is the calculated performance from a model that includes measured gains and optical transmissions of the system. The maximum 1ω energy and fluence demonstrated at 3, 5, and 8 ns are listed in Table 1.

The gain-performance curve shown in Fig. 10 does not depend on the temporal pulse shape. However, for this shot series, the input pulses were temporally shaped to give nearly square output pulses. Figure 11 shows an example of input and output temporal pulse shapes under highly saturated conditions with an output of 15.5 kJ in an 8-ns pulse. Under these conditions, the intensity of the leading edge of the input pulse is shaped to be 12.5 times the intensity of the trailing edge to maintain a square output pulse shape.

Near-Field Beam Features

All large glass lasers have intensity noise in the near field as a result of diffraction from small obscurations and flaws in the many optical components through which the beam passes. The operating limit of ICF glass lasers is often set by the peak of the near-field intensity noise because of the threat for optical damage. However, the output power of the laser is determined by the average intensity. Therefore it is desirable to have a peak-to-average intensity ratio as near to unity as possible.

Figure 12 shows the 1ω near-field image of the Beamlet output at 8 kJ and 3 ns. This represents the quality of the beam that is sent toward the frequency converter. The peak-to-average fluence modulation, due to diffractive noise sources, is about 1.3 to 1. For comparison, the Nova laser, when operated at high fluence, typically has a peak-to-average fluence modulation of about 1.5 to 1.

Some of the prominent patterns shown in the near-field image (Fig. 12) originate from identified sources. For example, the small obscurations near the center of the image are originally from optical breakdown in air paths caused by ghost reflections. Ghost reflections refer to the small reflections from antireflection (AR) coated optics. Because AR coatings are not perfect, some very small portion of the incident light is reflected. If these reflections originate from curved surfaces such as lenses, they will either diverge or come to a focus. The focused ghosts can be intense enough to cause optical breakdown in the air path of the beam or even optical damage if the focus occurs at or near an optical component. Ghost reflections from the Beamlet cavity spatial filter lenses come to a focus in air between the lens and the amplifier or Pockels cell where they cause small air breakdown plasmas to form. When the laser pulse returns through that region on a later pass, these ghost foci appear as small obscurations on the beam. The obscurations are much less apparent after the booster amplifier since they fill in due to unsaturated gain in that amplifier stage. Other features faintly visible in the

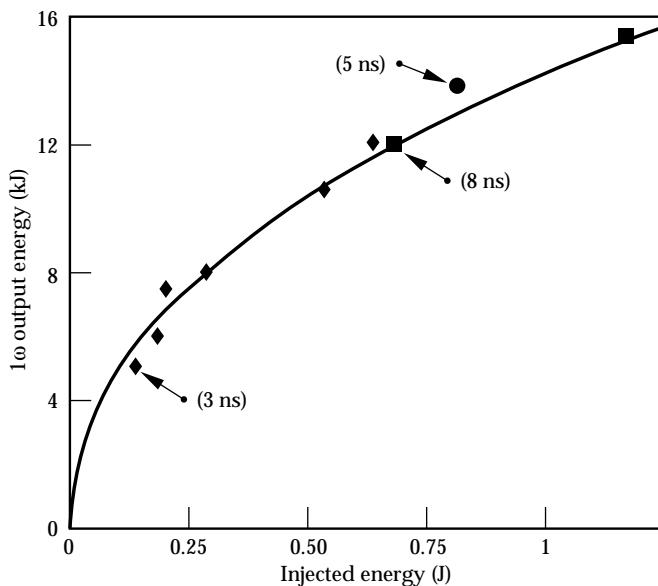


FIGURE 10. Measured 1ω output energy vs energy injected into the large multipass cavity. These tests were carried out with eleven amplifier slabs in the four-pass cavity and five in the singlepass booster amplifier (with a flash-lamp pump explosion fraction of 0.2). (70-50-1094-3626pb01)

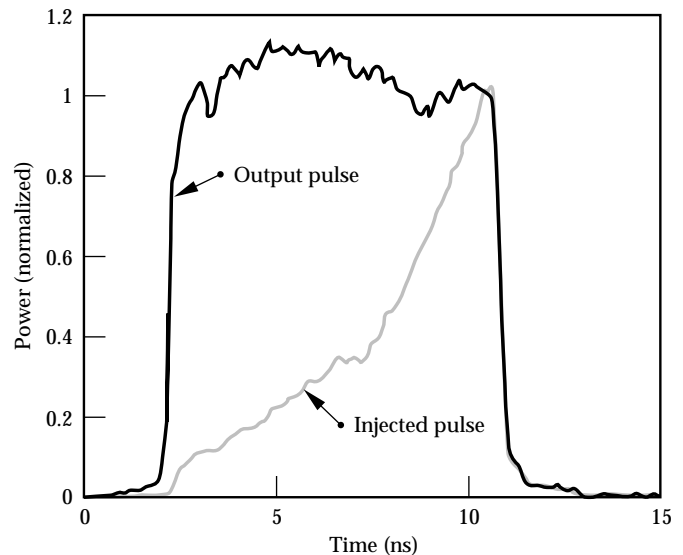


FIGURE 11. Comparison of 1ω input and output temporal profiles for a full-system shot (eleven- and five-amplifier slab configuration). The input energy is 1.2 J and the contrast ratio (ratio of the leading to trailing edge intensities) is about 12.5 to 1. The output energy is 15.5 kJ at 8 ns. (70-50-0195-0024pb01)

near-field image (Fig. 12) include multiple Airy patterns caused by small opaque defects. Nearly all of these originate from tiny particulates on some of the small optics of the diagnostic camera system.

Figure 13 shows the cumulative intensity distributions for image pixels within the flat-top area of the Beamlet output beam under several different conditions, illustrating the effects of saturation and modulation growth due to the nonlinear index of refraction in the optical components. Each pixel corresponds to a beam area of $1.4 \times 1.4 \text{ mm}^2$. The 8-ns pulse at 15.5 J/cm^2 or 1.94 GW/cm^2 has a steeper distribution function than the other shots plotted, particularly in the high-intensity regions. This shows the effect of gain saturation for high-intensity peaks, coupled with the absence of any significant nonlinear effects at this long pulse length and low intensity. The 3-ns pulse at 12 J/cm^2 or

4.0 GW/cm^2 shows some growth of intensity peaks due to nonlinear index; at high intensities, this nonlinear effect tends to amplify light scattered at small angles by defects in the optics.

Nonlinear Effects at High Intensity

At very high intensities, the intensity-dependent part of the refractive index becomes important. This nonlinear effect causes growth of noise (small angle scattering) by energy transfer from the main beam through a second-order wave mixing process.¹⁴ The gain of noise growth depends on its spacial frequency. This process limits the laser performance, because excessive growth of noise components can lead to damage of laser components. In Beamlet, beam breakup (due to small-scale self-focusing of noise spikes) limits the performance at and below 3 ns. Quantifying this effect on Beamlet is very important to confirm the theory and modeling, which also have been applied to establish the NIF performance.

These studies are hazardous for the laser components, however, because the intensity modulation can grow very quickly to damaging levels. To minimize the risk to the laser, we chose to study the growth of intensity modulation with short pulses (200 ps) and with the booster amplifier unpumped. Note that by using short pulses, we can propagate high-intensity beams at fluences far below the damage thresholds of the optical components. For these shots, the unpumped booster amplifier served as merely an array of nonlinear components in which we could study the growth of beam modulation.

The onset of significant small-scale self-focusing usually occurs when the intensity-driven, nonlinear

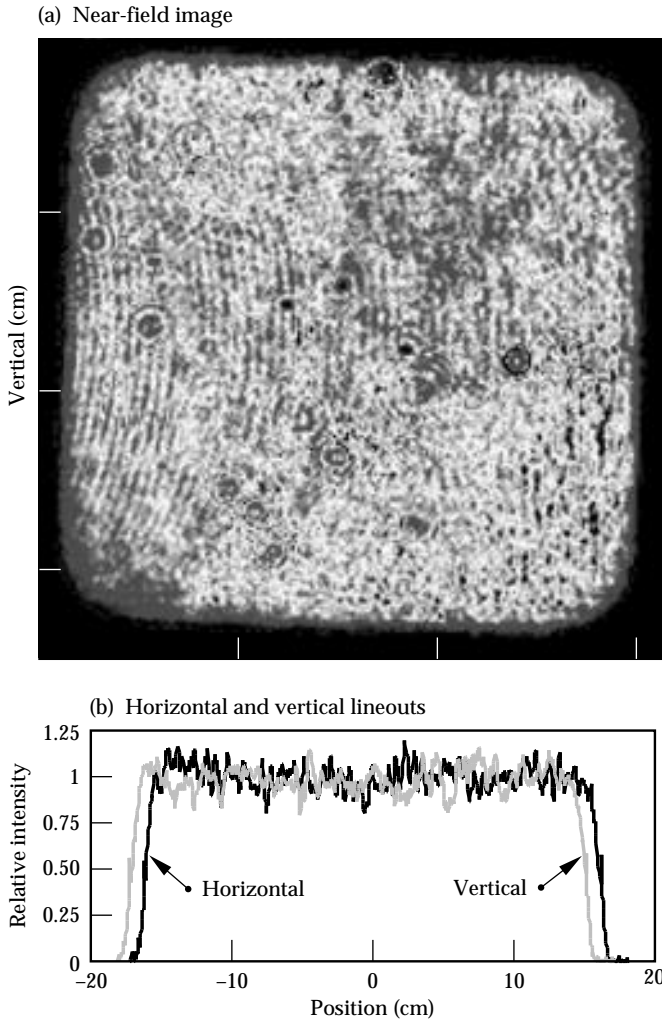


FIGURE 12. (a) Near-field image of the 1ω output from Beamlet for a 5.9-kJ shot at 3 ns; (b) Horizontal and vertical lineouts through the image. (70-50-0494-2124pb01)

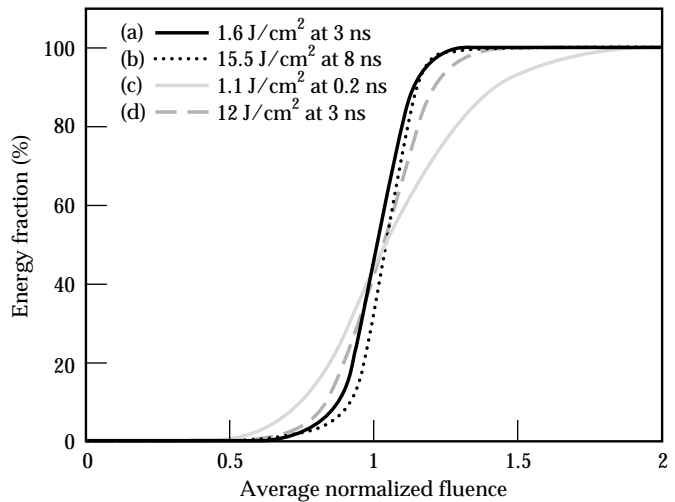


FIGURE 13. Cumulative 1ω intensity distributions determined from near-field image profiles for Beamlet shots at various pulse lengths and mean fluences. (a) 0.53 GW/cm^2 , (b) 1.94 GW/cm^2 , (c) 5.5 GW/cm^2 , and (d) 4.0 GW/cm^2 . (70-50-0195-0017pb01)

phase shift reaches about 2 rad. There is a noticeable growth of the intensity modulation in the $4.0\text{-GW}/\text{cm}^2$ image, and serious beam breakup has begun at $5.5\text{ GW}/\text{cm}^2$. Figure 14 shows the near-field appearance of the output beam at this intensity. The nonlinear phase shift through the Pockels cell and booster amplifier amounts to 3 rad for this shot. These shots were taken using the original KDP Pockels cell crystal that had a poor-diamond-turned surface and imposed a 6.4-mm period modulation on the beam. (See “Large-Aperture, High-Damage Threshold Optics for Beamlet,” p. 52 for a detailed discussion.) It is clear that this modulation serves as the noise source that seeds the nonlinear intensity growth and beam breakup.

1 ω Far-Field Beam Quality

The nominal NIF ignition target design requires a 0.5-mm-diam spot at the focus of a 7-m focal length lens.¹ Energy lying much outside this $\pm 35\text{-}\mu\text{rad}$ angle is not useful and can be harmful if it strikes the wrong area of certain targets. Some experiments planned for NIF require smaller spots, so a smaller beam divergence is desired. The diffraction limit of a normal 35-cm beam is $\pm 5\text{ }\mu\text{rad}$, so a NIF beamlet should be roughly 3 to 7 times the diffraction limit, as usually defined, at the fundamental $1.053\text{-}\mu\text{m}$ wavelength (this divergence is preserved when the beam is converted to the third harmonic). Efficient frequency conversion also sets a beam divergence specification,⁵ but it is less stringent than this spot size requirement for NIF ($\pm 35\text{ }\mu\text{rad}$).

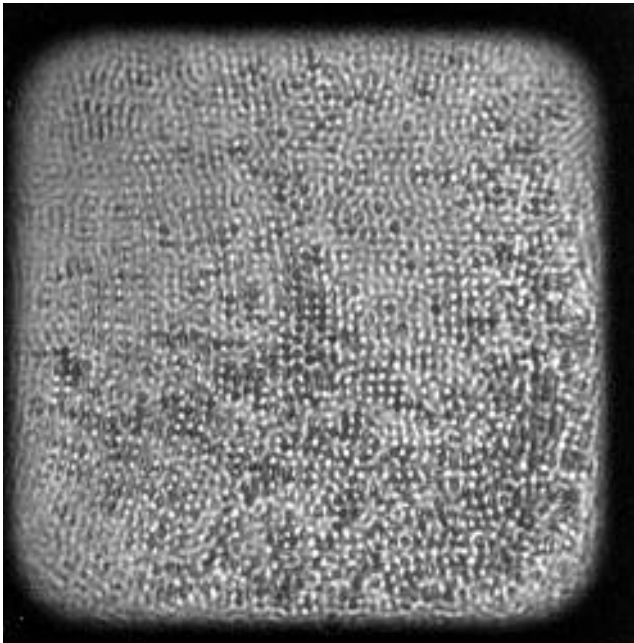


FIGURE 14. Near-field image of the 1ω output beam for a $5.5\text{-GW}/\text{cm}^2$ shot at a 200-ps pulse width. The white dots are hot spots with an intensity nearly twice the average intensity. Figure 13(c) shows the cumulative intensity distribution for this shot. (70-50-0195-0023pb01)

As mentioned earlier, a DFM is used on Beamlet to correct for low-order static and dynamic wavefront aberrations. (See “Beamlet Pulse-Generation and Wavefront-Control System,” p. 42.) Figure 15 shows a recent Beamlet 1ω far-field profile obtained using pre-correction for static and pump-induced aberrations on a 4.5-kJ 3-ns shot. The rms wavefront aberration is reduced to 0.17 waves, which leads to a calculated Strehl ratio of 0.4. The central spot is diffraction limited and approximately $10\text{-}\mu\text{rad}$ wide. Most of the energy is contained well within the NIF requirement of $\pm 25\text{-}\mu\text{rad}$ divergence angle. The booster amplifiers were not yet installed at the time this shot was taken. For comparison, the beam without wavefront correction by the DFM would almost fill the entire image plane shown in Fig. 15.

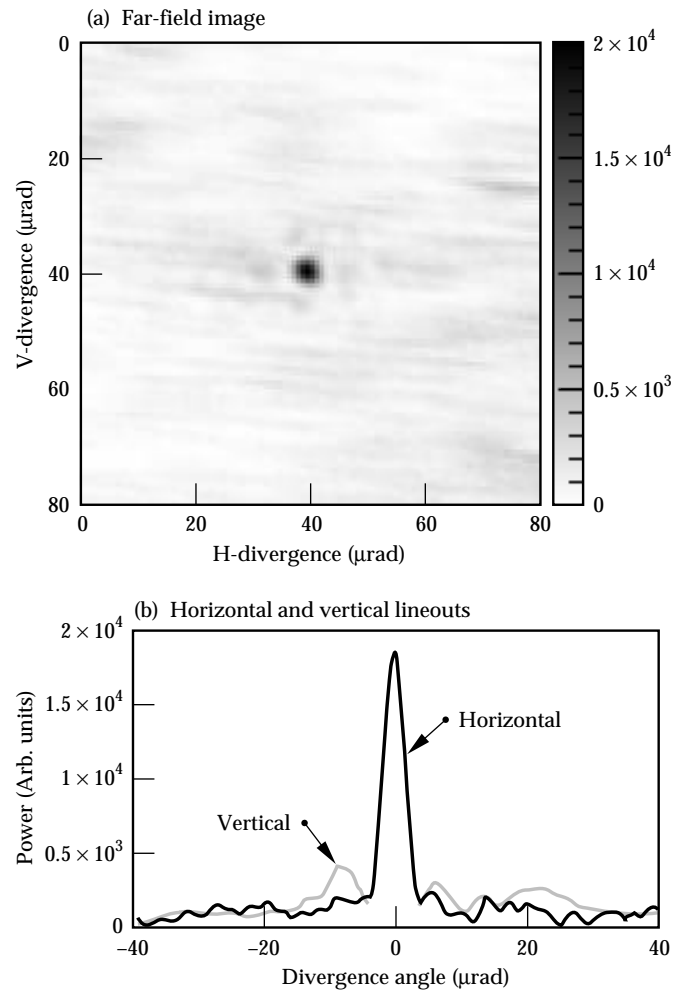


FIGURE 15. (a) 1ω far-field image and (b) horizontal and vertical lineouts of a 4.5-kJ 3-ns Beamlet shot. The wavefront of the $35 \times 35\text{ cm}^2$ beam was fully precorrected for static and pump-induced aberrations using a 39-element DFM. (70-50-0195-0023pb01)

Table 2 summarizes preliminary results obtained using the Beamlet Hartmann wavefront sensor and adaptive optics control system. The DFM corrects for the static aberration in the beamline, such that the output wavefront is nearly flat before a shot. The pump-induced wavefront aberration during a shot is largest near the edges of the beam and amounts to 1.65 waves peak-to-valley (p-V) for a 34-cm beam size.

Preliminary attempts to precorrect the injected wavefront for this dynamic distortion showed a reduction of the output aberration by a factor of two. The large and slowly decaying thermally induced aberration in the amplifier slabs after a shot can again be corrected in real time. These results clearly demonstrate the value of the adaptive optics system to increase the brightness of ICF lasers.

Harmonic Generation Experiments

Beamlet Frequency Conversion System

Third-harmonic generation on Beamlet was achieved by the sequential application of collinear sum-frequency mixing in two nonlinear crystals. A beam at the fundamental laser frequency is incident upon the first nonlinear crystal in which second-harmonic generation takes place via degenerate sum-frequency mixing ($\omega_2 = 2\omega_1$). Two copropagating beams, one at the fundamental and the other at the second harmonic, emerge from this “doubling” crystal. They are incident upon the second nonlinear crystal in which the fundamental and the second harmonic again interact through sum-frequency mixing to create a wave at the third harmonic. To efficiently transfer power from the incident waves to the higher harmonic requires that both waves traverse the crystal in phase. Two methods of phase matching are

possible—Type I phase matching, where the two input waves have the same polarization; and Type II phase matching, where the two input waves are orthogonally polarized. Details of the harmonic generation process are described elsewhere.^{15,16}

The Type I KDP second-harmonic generation crystal converts a large fraction of the 1054-nm light to the second harmonic at 532 nm. The Type II KD*P “tripling” crystal then converts this residual fundamental and the second-harmonic beam to the third harmonic at 351 nm. The efficiency with which the third harmonic is generated is very sensitive to the ratio of the intensities of the fundamental and the second-harmonic beams incident on the tripler. This mix ratio is controlled by the length of the doubling crystal and a slight mismatch between the propagation direction of the beam inside the doubling crystal and the perfect phase matching direction.

The Beamlet frequency conversion system is designed to hold two different sizes of square crystal plates (32 and 37 cm). These crystals can accommodate maximum beam sizes up to about 30 and 34.5 cm, respectively. We activated the frequency converter with 32-cm crystals, although 37-cm crystals will be installed and tested in early 1995. The smaller crystals were used in our initial tests because they became available about 6 months before the larger ones. This is simply due to the longer time needed to grow the 500-kg single-crystal boules from which the 37-cm plates were cut. (See “Large-Aperture, High-Damage Threshold Optics for Beamlet,” p. 52 for more details on the crystals.) The crystals are installed in two 61-cm-diam optical mounts that allow x and y translation, rotation about the axis of beam propagation, and tilt about two orthogonal axes in the plane of the crystal (Fig. 16). The crystals and their mounts are contained within an insulated housing that maintains the temperature to within ± 0.1 K and $\pm 10\%$ relative humidity.

TABLE 2. Measured 1 ω static and dynamic beam aberration on Beamlet.

Measurement Condition ^a	30-cm beam		34-cm beam	
	p-V ^b	rms	p-V	rms
Static aberration (cold cavity)	1.4	0.2	2.6	0.4
Dynamic aberrations starting with a corrected wavefront in a cold cavity				
• Preshot (~10 min)	0.11	0.03	0.13	0.04
• Shot without correction	0.69	0.22	1.65	0.39
• Shot with partial correction	0.50	0.17	0.72	0.20
• Post shot (~+10 min)	2.4	0.85	3.6	1.3

^aMeasured distortion (in waves at 1.05 μm).

^bPeak-to-valley.

The input and output surfaces of the conversion crystals were coated with a single-layer, quarter-wave-thick, SiO_2 sol-gel AR coating. To simplify the crystal AR-coating process, both the input and output faces of the doubler have an AR coating with optimum transmission at 700 nm. This provides a very good compromise for optimal transmission at both 1054 and 527 nm when using a single-layer AR coating. The output face of the tripler has an AR coating optimized at 351 nm, whereas the input face has an extra coating layer applied to produce the $1\omega/2\omega$ compromise coating thickness.

The tripling crystal was deuterated to reduce the potential for damage from stimulated Raman scattering (SRS). The intense spontaneous Raman band that occurs in KDP near 915 cm^{-1} (and seeds the SRS growth) is split into two weaker bands in KD^*P .¹⁷ In addition to

using KD^*P , we also beveled and AR-coated the edges of the crystal to prevent parasitic oscillations from SRS within the plane of the crystal and orthogonal to the beam propagation vector.

Second-Harmonic Generation

The frequency conversion system was activated in two stages. The $32 \times 32\text{-cm}^2 \times 1.05\text{-cm}$ -thick Type I doubling crystal was installed and the second-harmonic conversion efficiency was measured as a function of input intensity at the phase matching angle ($\Delta k = 0$). Experiments were carried out with increasing 1ω input intensities up to about 5.3 GW/cm^2 using 1-ns square pulses. The second-harmonic conversion efficiency increased monotonically with drive intensity, reaching a maximum value of 83%. These results

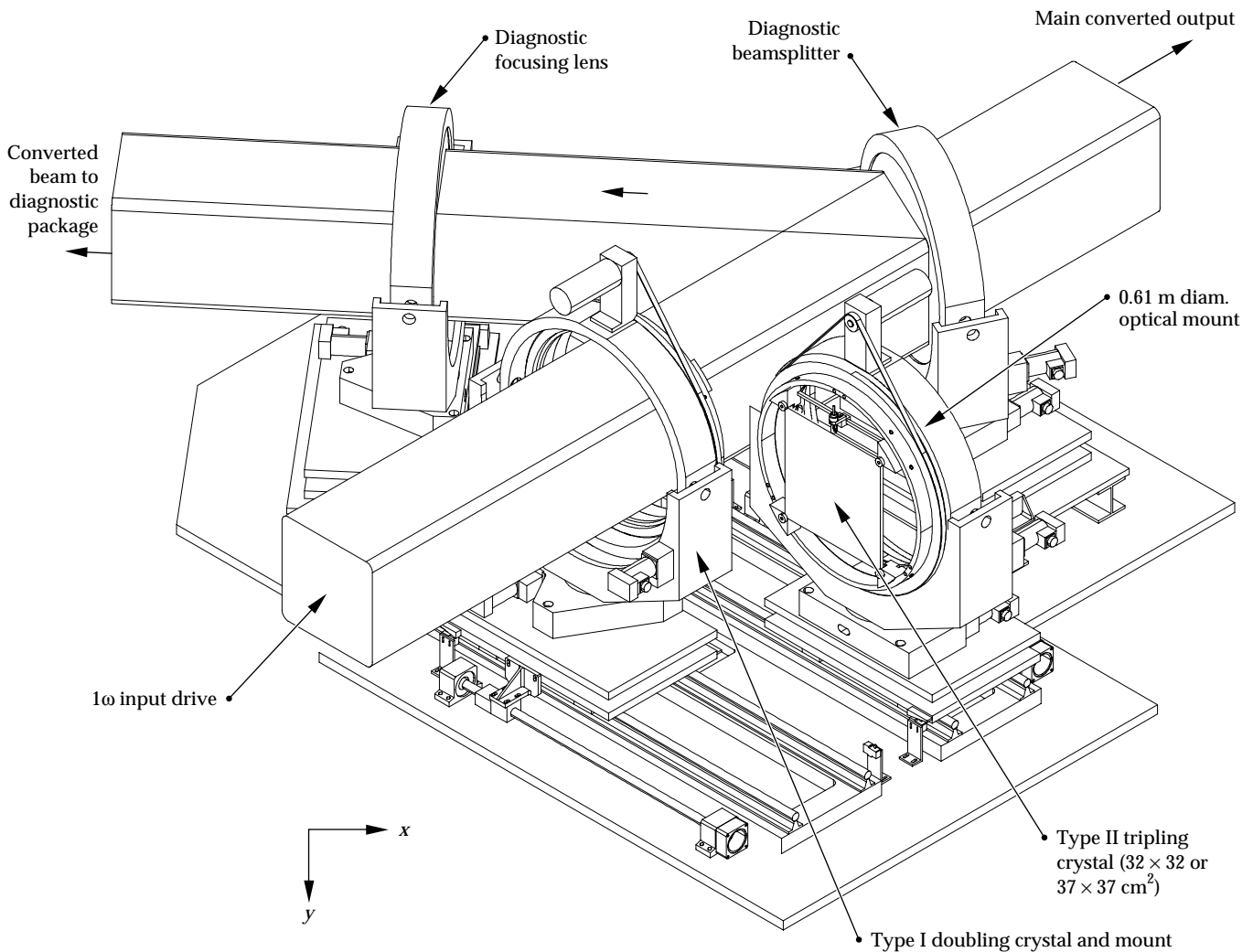


FIGURE 16. Layout of the third-harmonic frequency-conversion system showing the location of the crystals in the optical mounts. The crystals can be independently moved in and out of the beamline. (70-50-0494-1913pb01)

(Fig. 17) were compared with plane-wave model calculations and were found to be in excellent agreement. This attests to the nearly flat wavefront quality (i.e., low distortion) of the Beamlet 1ω drive beam.

The plane-wave model assumes a 1% loss at each AR-coated surface of the crystals and 6%/cm absorption at 1054 nm by the bulk KDP. As noted earlier in this section, the second-harmonic generation crystal is slightly “detuned” from the phase-matching angle to achieve the proper mix ratio of the fundamental and second-harmonic beam that drives the tripler. Theory predicts that a detuning angle of $\pm 250 \mu\text{rad}$ from the phase matching direction in the crystal will give the correct mix ratio to achieve maximum 3ω conversion at incident fundamental intensities between 3 and $3.5 \text{ GW}/\text{cm}^2$.

During the course of the doubling experiments, we also measured the conversion efficiency at detuning angles of ± 250 and $350 \mu\text{rad}$ and compared the results

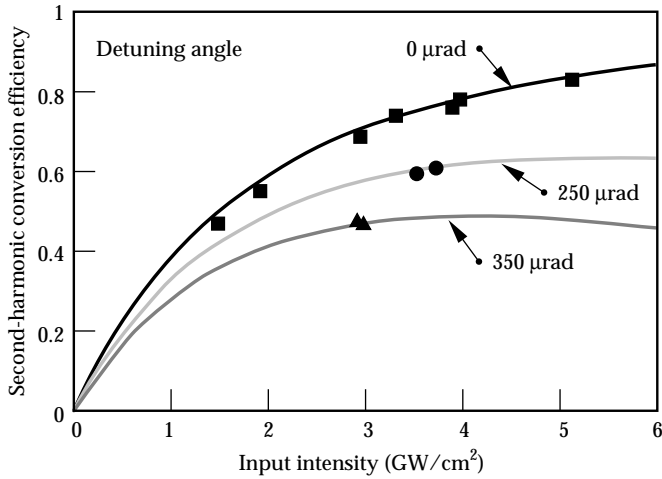


FIGURE 17. Second-harmonic conversion efficiency vs 1ω drive intensity using a $32 \times 32 \times 1.1 \text{ cm}^3$ KDP Type I doubling crystal. The conversion efficiency agrees well with the plane-wave model at 0, ± 250 , and $\pm 350 \mu\text{rad}$ detuning angles. (70-50-1094-3625pb01)

with the plane-wave model (Fig. 17). Again, the agreement between the model and experiment was very good. To do these conversion tests, the doubling crystal was first tilted (detuned) to one side and the conversion efficiency measured. This experiment was then repeated with the crystal tilted an equivalent amount in the opposite direction. Thus, the two points shown in Fig. 17 at each of the detuning angles represent two separate experiments where the crystal was detuned by either “plus” or “minus” the respective angle.

Third-Harmonic Generation

Table 3 summarizes the results from third-harmonic generation experiments carried out with a 3-ns square pulse shape. These results are compared with both the NIF requirements and the Beamlet performance goal established at the beginning of the project at the recommendation by the National Academy of Sciences (NAS).

Beamlet is judged against three key third-harmonic performance criteria: (1) fluence, (2) beam quality, and (3) conversion efficiency. For all three criteria, Beamlet either exceeds or meets the goals of the NIF (see Table 3). The difference in total output energy proposed for a NIF beamlet vs that achieved on the prototype Beamlet is due to the difference in aperture size. The prototype Beamlet aperture was set at the beginning of the project in 1991 and supports a maximum beam size of 35 cm. On the other hand, the somewhat larger NIF aperture reflects the more recent thinking that apertures near 40 cm, rather than 30 cm, are a better compromise between performance and cost.

Perhaps the most critical performance criteria is the 3ω fluence, because of the lower optical-damage limits at shorter wavelengths. Specifically, the optical material most at risk is the tripling crystal, because the laser output is set to be near the damage threshold of this material. Beamlet has operated at a 3ω fluence that exceeds the NIF performance requirement by about 10%. During these initial tests, we carried out 17 shots

TABLE 3. Comparison of Beamlet 3ω performance with NIF and the NAS technical contract specifications.

Parameters	Beamlet Phase I ^a	NIF	NAS technical contract
Mean 3ω fluence J/cm^2	8.7	8.0 ^b	6.4–7.6
Quality:			
• Beam size (cm^2)	29.6×29.6	38×36	30×30
• Effective beam area (cm^2)	736	1280	784
• 3ω energy (kJ)	6.4	10.2	5–6
• Beam divergence (μrad)	$\leq \pm 25$	$\leq \pm 35$	$\leq \pm 50$
• Bandwidth (GHz)	90	90	90
Conversion efficiency:			
3ω peak conversion efficiency	80%	80%	70%

^aSee Ref. 18.

^bat 3.6 ns.

in excess of 7.5 J/cm^2 at 3 ns without sustaining any damage to the K*DP tripling crystal.

The third-harmonic converter was activated by first “laser conditioning” the KD*P tripling crystal at 3ω . Laser conditioning refers to the process of increasing the damage threshold of an optical material by exposing it to a series of laser shots with monotonically increasing fluence. (See “Large-Aperture, High-Damage Threshold Optics for Beamlet,” p. 52 for a detailed discussion of laser conditioning of Beamlet optics.) Following conditioning, a series of experiments was conducted to characterize the 3ω conversion performance. One of our major goals was to demonstrate $>70\%$ conversion efficiency at high peak power ($2.5\text{--}3.5 \text{ GW/cm}^2$). These experiments were carried out using temporally square, 3-ns pulses. Figure 18 shows the results where the third-harmonic conversion efficiency is plotted vs the 1ω input intensity delivered to the harmonic converter system. At the highest drive intensities ($>3.25 \text{ GW/cm}^2$) conversion efficiencies of 80% were achieved. The results were in good agreement with plane-wave model predictions. The model calculations include the effects of the 30-GHz bandwidth (90-GHz at the 3ω output) that we add to the drive pulse to suppress SBS in the output optics. The added bandwidth reduces the conversion efficiency about 3% at the highest drive intensities. The model calculation shown in Fig. 18 does not include the effects of the spatial and temporal edges of the real beam, but instead assumes a perfect top-hat-shaped profile. Including these effects would tend to slightly reduce the

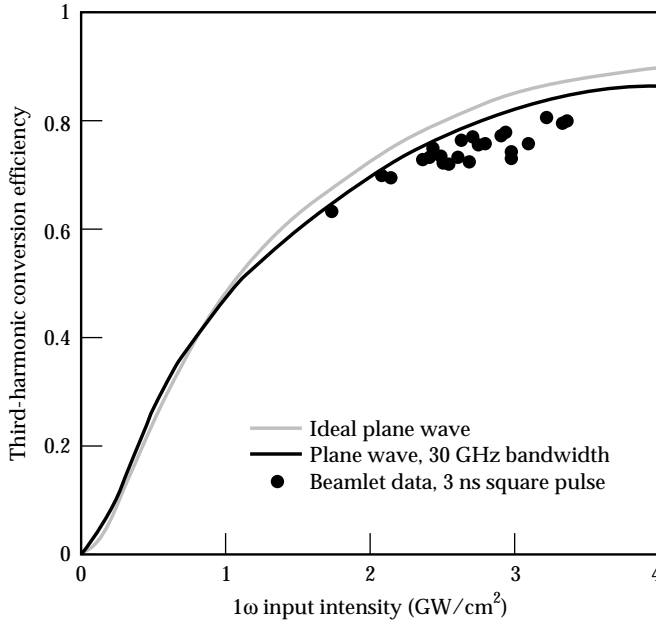


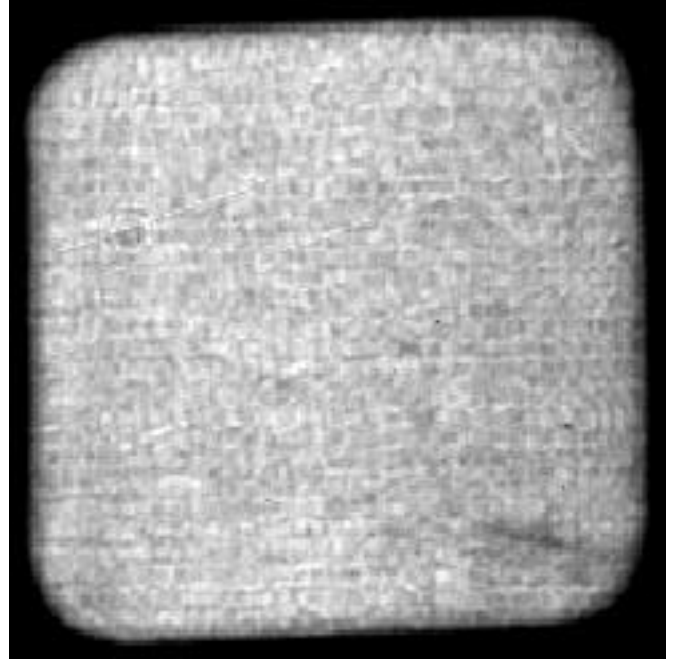
FIGURE 18. Third-harmonic conversion efficiency vs 1ω drive intensity achieved with 3-ns square pulses with 30-GHz 1ω (90-GHz at 3ω) bandwidth. The Type II tripling crystal was 80% deuterated KD*P $32 \times 32 \times 0.95 \text{ cm}^3$ with 0 μrad detuning. The doubling crystal was detuned at $\sim 250 \mu\text{rad}$ to achieve optimum 3ω conversion. (70-50-1094-3624pb01)

conversion efficiency, giving even closer agreement with the experiments.

The maximum average 3ω output fluence achieved during this series of shots was 8.7 J/cm^2 , about 10% greater than the NIF performance goal of 8.0 J/cm^2 . At the Beamlet beam aperture area of 736 cm^2 , this gave 6.4 kJ 3ω output and corresponds to over 11 kJ at the NIF beam area of 1280 cm^2 (Table 3).

The input beam quality and fill factor were maintained during the 3ω conversion process as shown by the 3ω near-field image and lineout in Fig. 19. These data were taken during a 3-ns shot at 2.56 GW/cm^2 producing 7.7 J/cm^2 (5.6 kJ) output at 3ω . The peak-to-mean intensity modulation is about 1.4 to 1 at 3ω compared to about 1.3 to 1 at 1ω .

(a) Near-field image



(b) Horizontal and vertical lineouts

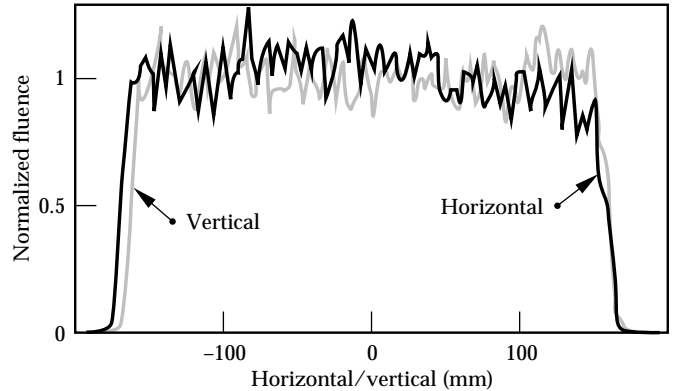


FIGURE 19. (a) Near-field image and (b) horizontal and vertical intensity lineouts of that image for a 3ω output pulse from the Beamlet harmonic generator. The peak-to-mean intensity modulation is about 1.35 to 1. (70-50-0195-0021pb01)

Figure 20 further illustrates the similarity in the fluence modulation observed for the 1 and 3ω near-field images at high drive intensities. Plotted is the normalized probability distribution of fluences observed at 1 and 3ω for a 3-ns shot. The average pulse intensities are 3.3 GW/cm^2 and 2.65 GW/cm^2 at 1 and 3ω , respectively. The wings of the two curves compare the p-V intensity distribution for the 1 and 3ω pulses. The data clearly show that there is no significant growth in near-field fluence modulation during the conversion process.

During the course of our 3ω tests, we also demonstrated frequency conversion for shaped pulses roughly similar to NIF ignition target drive pulses. The proposed NIF ignition target pulse shape consists of a low-intensity “foot” about 15 ns long followed by a higher intensity, 3–3.5-ns, main drive pulse. The harmonic conversion process depends strongly on the product of the beam intensity and crystal thickness and therefore has a limited intensity range over which it is fully optimized. This is illustrated by the data in Fig. 18, where the conversion efficiency is shown to drop-off dramatically at low-drive intensity; in this case, the crystals are optimized for intensities in the range of $2\text{--}5 \text{ GW/cm}^2$. In both the NIF and prototype-Beamlet design, the conversion efficiency of the foot will be lower than the main pulse. The NIF requirement is 60% conversion efficiency for the nominal ignition pulse shape. Because the Beamlet preamplifier section was designed to handle a maximum pulse length of 10 ns, we simulated a complex pulse shape (similar to what might be used on NIF) using a 7-ns foot and a 3-ns main pulse. The 1ω input to the harmonic converter had a foot-to-main pulse contrast ratio of 9:1, giving the desired 30:1 contrast ratio for the 3ω output pulse (Fig. 21). The 1ω beam had an equivalent pulse length of 3.9 ns and a mean fluence of 12.4 J/cm^2 compared with 3.2 ns and 8.2 J/cm^2 for the output 3ω pulse. The measured foot

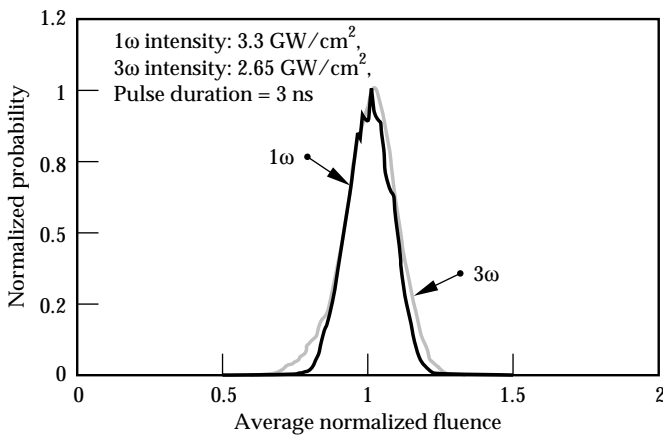


FIGURE 20. Comparison of normalized probability distribution of intensities for the 1ω drive pulse and corresponding 3ω output observed during a 3-ns shot at a 1ω input drive intensity of 3.3 GW/cm^2 . (70-50-0195-0019pb01)

and peak pulse conversion efficiencies were 23 and 77%, respectively. The average 3ω conversion efficiency was 64%, which compares quite favorably with our model predictions.

The above 3ω experiments also gave us the added opportunity to more fully test the capability of the integrated optical-pulse forming and preamplifier section of our front end. To create the desired 9:1 1ω NIF-like pulse shape that was used to drive the harmonic converter requires nearly a 75:1 intensity contrast for the shaped pulse at the injection to the main laser cavity [Fig. 21(b)]. The injected pulse was shaped to compensate

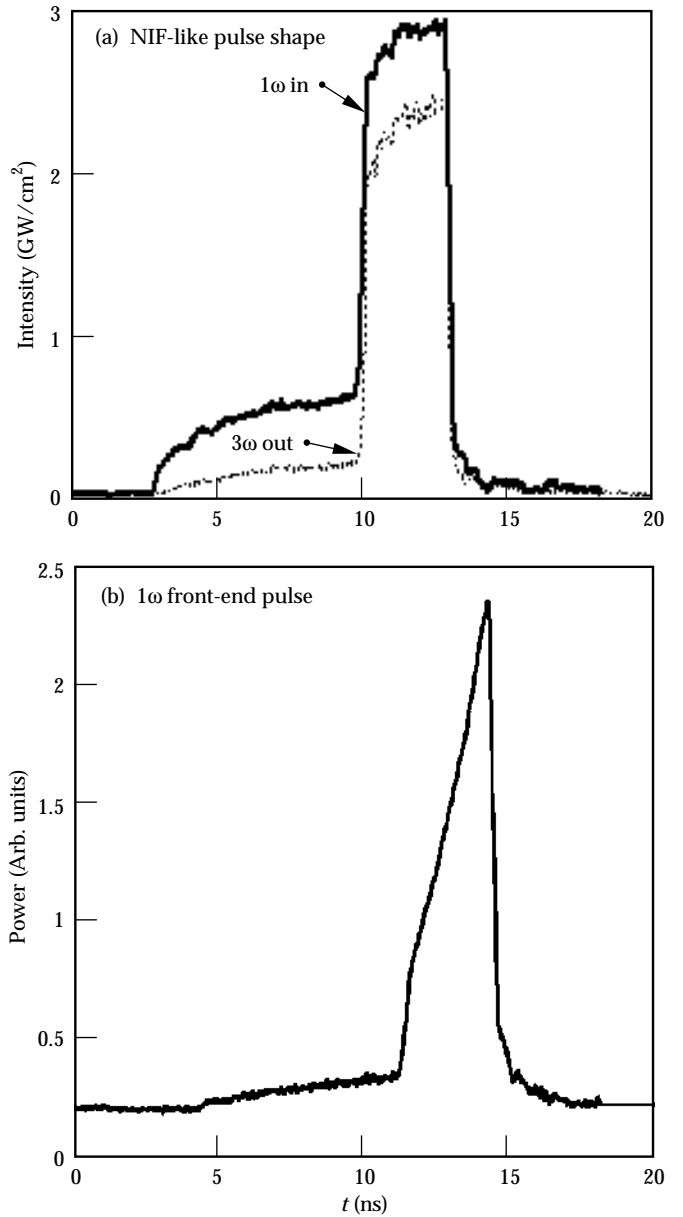


FIGURE 21. (a) Shows a “NIF-like” 3ω pulse shape with a 30:1 contrast ratio generated using a 9:1 1ω drive pulse to the harmonic converter. (b) An injected pulse with a 75:1 contrast and a complex temporal shape was generated using the new front-end architecture to achieve the desired 1ω drive-pulse shape. (70-50-1094-3622pb01)

for effects of gain saturation in the main laser cavity and booster amplifiers. This pulse shape was easily synthesized using the low-voltage waveguide modulators in the pulse generation system.

Summary

We recently completed construction and preliminary testing of the NIF prototype Beamlet laser, a large-aperture flash-lamp-pumped Nd:Glass laser. The laser uses a multipass architecture that represents the first attempt to employ such a design at this scale. The main laser cavity is unique in that it uses a full-aperture plasma-electrode Pockels cell and an angular multiplexing scheme to execute four passes through a group of eleven large phosphate glass amplifiers contained in the cavity. The output from the main laser cavity then makes a single pass through a booster amplifier section comprised of five more amplifiers. The 1054-nm output from the laser is converted to the third harmonic (351 nm) using a Type I/II KDP/KD*P frequency conversion scheme.

We have successfully demonstrated Beamlet's 1ω and 3ω performance at its 3-ns design point. Good beam quality is maintained as defined by the low peak-to-average fluence modulation and small wavefront aberration. We demonstrated several new pre-compensation techniques in the preamplifier that allow control over fill factor, wavefront, and temporal shape of the output beam. Key 1ω performance parameters have been investigated at high 1ω fluence (15.5 J/cm^2), and high intensity (5.5 GW/cm^2). Similarly, at 3ω we demonstrated damage-free operation at fluences in excess of those required for NIF and third-harmonic conversion efficiencies $>80\%$ for 3-ns pulses and 64% for NIF-like pulse shapes. The conversion efficiencies mentioned exceed NIF requirements. The results from current and future Beamlet performance tests will be used to validate the NIF laser design.

Acknowledgments

We gratefully acknowledge the contributions of the many LLNL engineers, technicians, scientists, and support personnel whose long hours and tireless efforts made this project possible. We also appreciate the high-quality, state-of-the-art optical, electrical, and mechanical components delivered by numerous vendors, including Aerotech Inc., Aerovox Inc., Cleveland Crystals, Inc., Corning, Eastman Kodak Company, EG&G Inc., Passat Enterprises, Schott Glass Technologies Inc., Spectra-Physics, Tinsley Laboratories, Inc., United Technologies, and Zygo Corporation.¹⁹⁻³⁰

Notes and References

1. *National Ignition Facility Conceptual Design Report*, 2 and 3, Lawrence Livermore National Laboratory, Livermore, CA, UCRL-PROP-117093 (May 1994).

2. A. C. Erlandson, K. S. Jancaitis, R. W. McCracken, and M. D. Rotter, *ICF Quarterly Report* 2(3), 105-114, Lawrence Livermore National Laboratory, Livermore, CA, UCRL-LR-105821-92-3 (1992).
3. B. M. VanWanterghem, D. R. Speck, M. Norman, R. B. Wilcox, et al., "A Compact and Versatile Pulse Generation and Shaping Subsystem for High Energy Laser Systems," in *Laser Coherence Control: Technology and Applications*, (SPIE—International Society for Optical Engineering, Bellingham, WA, 1993; *Proc. SPIE* 1870).
4. M. A. Rhodes, J. J. DeYoreo, B. W. Woods, and L. J. Atherton, *ICF Quarterly Report* 2(1), 23-36, Lawrence Livermore National Laboratory, Livermore, CA, UCRL-LR-105821-92-1 (1992).
5. C. E. Barker, D. Milam, and R. Boyd, *ICF Quarterly Report* 3(2), 55-62, Lawrence Livermore National Laboratory, Livermore, CA, UCRL-LR-105821-93-2 (1993).
6. J. R. Murray, J. H. Campbell, D. N. Frank, J. T. Hunt, and J. B. Trenholme, *ICF Quarterly Report* 1(3), 89-107, Lawrence Livermore National Laboratory, Livermore, CA, UCRL-LR-105821-91-3 (1991).
7. J. T. Hunt and D. R. Speck, *Optical Engineering* 28(10), 461-468 (1989).
8. J. M. Soares, R. C. McCrory, T. R. Boehly, R. S. Craxton, et al., *Laser and Particle Beams* 11, 317-321 (1993).
9. C. Yamanaka, *Lasers and Particle Beams* 2, 425-431 (1984).
10. G. Thiell, A. Adolf, M. Andre, N. Fleurot, et al., *Laser and Particle Beams* 6, 93-103 (1988).
11. J. R. Murray, J. R. Smith, R. B. Ehrlich, D. T. Kyrasiz, et al., *J. Opt. Soc. Am. B* 5, 2402 (1989).
12. J. T. Salmon, E. S. Bliss, T. W. Lang, et al., (SPIE—International Society for Optical Engineering, Bellingham, WA, 1991; *Proc. SPIE* 1542) p. 452.
13. J. M. Auerbach and V. P. Karpenko, *Applied Optics* 33(15), 3179-3183 (1994).
14. E. S. Bliss, D. R. Speck, J. F. Holzrichter, J. H. Eskkila, and A. J. Glass, *Appl. Phys. Lett.* 25, 448-450 (1979).
15. J. A. Armstrong, N. Bloembergen, J. Ducuing, and P. S. Pershan, *Phys. Rev.* 127, 1918-1939 (1962).
16. R. S. Craxton, *Opt. Commun.* 34(3), 474-478 (Sept 1980).
17. R. A. Sachs, C. E. Barker, and R. B. Ehrlich, *ICF Quarterly Report* 2(4), 179-188, Lawrence Livermore National Laboratory, Livermore, CA, UCRL-LR-105821-92-4 (1992).
18. Beamlet Phase I is the Beamlet integration and activation leading to the 1ω and 3ω performance as described in this article. Beamlet Phase II, which started in November 1994, is the expansion of the present configuration to one which mimics a full NIF beamline, including a 3ω focusing vessel, similar to a section of the NIF target chamber, to diagnose on-target performance.
19. Aerotech Inc., 101 Zeta Drive, Pittsburgh, PA, 15238.
20. Aerovox Inc., 740 Belleville Avenue, New Bedford, MA, 02745-6194.
21. Cleveland Crystals, Inc., 676 Alpha Drive, Highland Heights, OH, 44143.
22. Corning, Corning Glass Works, MP-21-04-2 Corning, NY, 14831.
23. Eastman Kodak Company, Department 177, Building 601, Rochester, NY, 14650-0803.
24. EG&G, Inc., Electro-Optics Division, 35 Congress Street, Salem, MA, 01970.
25. Passat Enterprises, P.O. Box 84, Nizhny Novgorod, Russia, 603000.
26. Schott Glass Technologies Inc., 400 York Avenue, Duryea, PA, 18642.
27. Spectra-Physics, 1330 West Middlefield Road, Mountain View, CA, 94039-0517.
28. Tinsley Laboratories Inc., 3900 Lakeside Drive, Richmond, CA, 94806.
29. United Technologies, Adaptive Optics Associates Inc., 54 Cambridge Park Drive, Cambridge, MA, 02140-2308.
30. Zygo Corporation, Laurel Brook Road, Middlefield, CT, 06455-0448.